Connecting the macroscopic and mesoscopic properties of sintered silver nanoparticles by crystal plasticity finite element method

Long, Xu; Chong, Kainan; Su, Yutai; Du, Leiming; Zhang, Guoqi

DOI
10.1016/j.engfracmech.2023.109137

Publication date
2023

Document Version
Final published version

Published in
Engineering Fracture Mechanics

Citation (APA)
Long, X., Chong, K., Su, Y., Du, L., & Zhang, G. (2023). Connecting the macroscopic and mesoscopic properties of sintered silver nanoparticles by crystal plasticity finite element method. *Engineering Fracture Mechanics*, *281*, Article 109137. https://doi.org/10.1016/j.engfracmech.2023.109137

Engineering Fracture Mechanics 281 (2023) 109137

Contents lists available at ScienceDirect

Engineering Fracture Mechanics

journal homepage: www.elsevier.com/locate/engfracmech

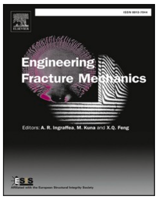

Connecting the macroscopic and mesoscopic properties of sintered silver nanoparticles by crystal plasticity finite element method

Xu Long [a,*], Kainan Chong [a], Yutai Su [a,*], Leiming Du [b], Guoqi Zhang [b]

[a] School of Mechanics, Civil Engineering and Architecture, Northwestern Polytechnical University, Xi'an, China
[b] Department of Microelectronics, Delft University of Technology, Delft, Netherlands

ARTICLE INFO

Keywords:
Sintered silver nanoparticle
CPFEM
Constitutive model
Initial orientation
Grain size

ABSTRACT

The stress–strain response of sintered silver nanoparticles (AgNP) materials is precisely characterized in order to adapt for numerical analysis and rational design of electronic packaging structures in this study. A framework of crystal plasticity finite element method (CPFEM) is established based on the mechanism of crystal plastic deformation to describe the mesoscopic structural influence of grain evolution on the macroscopic properties of sintered AgNP materials. Material parameters of crystal plasticity are defined and initial orientations are randomly assigned for sintered AgNP grains. To calibrate the mesoscopic mechanical properties of sintered AgNP by the proposed CPFEM, the results of CPFEM simulations and uniaxial tensile tests subjected to different strain rates and temperatures are compared in terms of the stress–strain curves as the critical macroscopic characteristics. The predicted stress and deformation distributions in the polycrystalline structure demonstrate that the significant inhomogeneity of stress and deformation is caused by the different grain orientations of sintered AgNP. Furthermore, we elucidate the fracture mechanism influenced by the temperature and strain rate and also the effect of initial crystal orientation on the plastic strain of sintered AgNP. This study sheds light on the morphology design of sintered AgNP with optimized mechanical properties and fatigue resistance.

1. Introduction

Traditional constitutive models have made remarkable achievements in investigating the macroscopic mechanical behavior of metal materials. For example, the Anand model [1–3] and unified creep plasticity model [4–9] have been used to describe the stress–strain response of viscoplastic materials at different temperatures and strain rates. From mesoscopic scale, significant heterogeneity of strain and stress often occurs in the internal grains of metal materials during the plastic deformation under the external loadings [10]. The plastic deformation of metal materials is essentially the result of the slip and twinning of grains [11]. Thus, the macroscopic constitutive models are incapable of taking account of the effect of grain characteristics on the *meso*-scale deformation and failure behavior of metal materials during plastic deformation. To bridge this gap, the crystal plasticity (CP) theory was successfully proposed and developed to reveal the cross-scale effects of mesoscopic structural evolution on the macroscopic stress–strain response of materials. As the fundamental basis, the plastic shear strain was introduced into the CP theory to describe the dislocation motion of crystalline materials [12]. One of the earliest applications of CP theory was to describe the interaction between single

---

[*] Corresponding authors.
E-mail addresses: xulong@nwpu.edu.cn (X. Long), suyutai@nwpu.edu.cn (Y. Su).

https://doi.org/10.1016/j.engfracmech.2023.109137
Received 19 December 2022; Received in revised form 12 February 2023; Accepted 14 February 2023

crystals in polycrystalline materials and the physical properties of single crystals during elasto-plastic deformation [13,14]. Since then, the well-known Schmidt's law [15], the rate-independent single crystal plastic constitutive model [16,17], the rate-dependent constitutive model [18,19] as well as the self and latent hardening model [20] have been established.

The crystal plasticity finite element method (CPFEM) combining finite element (FE) analysis and CP theory has been widely adopted along with the unceasing development of FE technology for studying the *meso*-scale deformation of crystalline materials [21]. Regarding the recent studies on CPFEM, Jiang *et al.* [22] found that the size dependence of polycrystalline grains could be predicted by a multi-scale strategy based on CPFEM. Dindarlou *et al.* [23] determined the low and high sensitivity parameters through a large number of experiments and improved the CP model based on *meso*-scale dislocation substructure to independently characterize the material parameters. Wang *et al.* [24] predicted the hot spots of crack nucleation during the fretting fatigue loading based on CPFEM by considering the mesoscopic structural characteristics of metals such as grain size, grain orientation and dislocation slip. In their study, the submodel technique was used to overcome the size limitation and minimize the influence of boundary conditions. Combining scanning electron microscopy and electron backscatter diffraction, Sonawane *et al.* [25] investigated the effect of grain boundary slip on the structural integrity of Cu Through Silicon Via (TSV) by using CPFEM. Their results showed that large shear stress was generated along the Cu grain boundary during annealing, which led to grain boundary slipping. By using anisotropic continuum damage mechanics and the rate-dependent CP theory, Amelirad *et al.* [26] studied the damage initiation and growth process of polycrystals. To date, the CPFEM has been proposed to elucidate the mesoscopic underlying mechanisms for the macroscopic loading bearing capacity and its deterioration for various engineering materials.

In the rapidly developing microelectronic packaging industry, higher requirements of mechanical reliability are expected on novel electronic packaging materials. This makes CPFEM an appealing method to numerically simulate and design the mesoscopic characteristics of packaging materials. Sasaki *et al.* [27] observed the slip lines of β-Sn crystals and simulated the strain distribution based on Hill's anisotropy theory and CP theory. It was shown that crystal deformation predicted by CPFEM was more accurate than Hill's anisotropy theory. Jin *et al.* [28] also found that CPFEM was more effective in predicting the fatigue life of sintered AgNPs compared with the OW-AF model. Furthermore, it was found that the grains near the pores had greater deformation, which means the existence of pores was likely to affect the deformability of the polycrystalline model. Xie *et al.* [29,30] described the temperature characteristics and rate-dependent effect of SAC305 solder on the deformation behavior based on CPFEM by modifying the reference slip strain rate $\dot{\gamma}_0$, critical resolved shear stress τ_0 and the rate-dependent sensitivity coefficient *n*. Furthermore, a dual-phase CPFEM model, including eutectic phase and β-Sn dendritic grains, was developed to simulate the thermal aging effect of SAC305 solder, which could predict the potential fault location of micro-sized solder joints. Zhang *et al.* [31] investigated the effects of grain orientation, grain boundary, and mesoscopic structural characteristics of intermetallic on the fatigue behavior of sn-rich solder joints under thermal cycling load by using CPFEM. Xu *et al.* [32] proposed a multi-scale modeling approach to study the Sn crystal orientation and its role in fatigue damage during thermal cycling. Based on these reviews of recent literature on packaging materials, it is apparent that CPFEM greatly facilitates the establishment of the relationship between the *meso*-scale deformation mechanism and the macro-scale deformation response of crystalline materials.

In addition to the conventional sn-based solder materials, active researches are ongoing for advanced packaging materials for harsh service conditions such as high temperatures. By identifying the sintered silver nanoparticle (AgNP) pastes as one of the promising candidates for die-attach materials of power electronics, their *meso*- and macro-scale mechanical properties have been attracting considerable attention. Long *et al.* [33] investigated the correlation between the microstructure and macroscopic constitutive behavior of sintered AgNP at different strain rates using a Berkovich indenter with a penetration depth of 2000 nm. Furthermore, the macroscopic constitutive behavior of sintered AgNP is established by performing dimensionless analysis based on the critical variables of nanoindentation response [34–36]. To achieve reliable and long-term service capability, the fracture behavior of sintered AgNP joints has been widely concerned under various loading conditions. The shear fracture toughness of sintered AgNP joints with different surface metal layers under different loading conditions has been investigated by numerous works [37–40]. Particularly, Chen *et al.* [41] found that the fracture toughness decreased with decreasing specimen size of sintered AgNP. Kim *et al.* [42] investigated the influence of bonding temperature on the microstructure and fracture behavior of sintered AgNP joints. In terms of numerical simulation, the phase-field fracture model for fracture is promising to simulate the crack initiation and fracture behavior in sintered AgNPs. Zhu *et al.* [43] investigated the crack growth process of sintered AgNP materials with various porosities based on the phase-field model. Su *et al.* [44,45] proposed a reliable phase-field technique to accurately depict the pore microstructure and predicted the fracture evolution process of sintered AgNPs.

Nevertheless, there is still a gap between *meso*-scale deformation and the macro-scale failure mechanism. To date, there are limited researches to address the relationship between grain characteristics and macroscopic behavior of sintered AgNP by using the CP model. In this study, the CPFEM is adopted to simulate the crystal deformation of sintered AgNP by proposing a polycrystalline FE model created with the Voronoi technology in order to unveil the fundamental relationship between *meso*- and macro- deformation responses of sintered AgNP. To calibrate the mesoscopic mechanical properties, the uniaxial tensile tests of sintered AgNP subjected to different strain rates and temperatures are simulated by the proposed CPFEM. The predicted distribution of von Mises stress and critical resolved shear stress are analyzed. Furthermore, the influence of the average grain size and its initial orientation are studied on a statistical basis by revealing the deformation mechanism of crystalline materials at the mesoscopic scale.

2. Framework of crystal plastic constitutive model

Different from the conventional constitutive model, the CP model has embedded parameters related to slip characteristics of crystalline materials, so as to describe the yield strength, shear stress, plastic strain, etc. of different slip systems during the deformation of crystal in detail. Therefore, it is significant to unveil the mesoscopic deformation mechanism of sintered AgNP by adopting the CP model. As shown in Fig. 1, the CP theory indicates that crystal deformation occurs from the initial configuration to the intermediate configuration due to the dislocation motion and then transforms to the current configuration caused by the lattice distortion and rotation. Therefore, the total deformation gradient $\boldsymbol{F}$ of the crystal including the elastic and plastic deformation [46] is decomposed by

$$\boldsymbol{F} = \frac{\partial \boldsymbol{x}}{\partial \boldsymbol{X}} = \boldsymbol{F}^{*}\boldsymbol{F}^{P} \tag{1}$$

where $\boldsymbol{x}$ is the particle coordinates in the current configuration, and $\boldsymbol{X}$ is the particle coordinates in the initial configuration. By following the simplification assumed by Huang [47], $\boldsymbol{F}^{*}$ denotes the elastic deformation gradient due to the lattice distortion and rotation, while $\boldsymbol{F}^{P}$ denotes the plastic deformation gradient due to the plastic shear deformation from the initial to the intermediate configuration in which lattice orientation and spacing are the same as in the initial configuration. In addition, $\boldsymbol{F}^{*}$ is decomposed into the product of the rotation tensor $\boldsymbol{R}^{*}$ and the stretching tensor $\boldsymbol{U}^{*}$ representing lattice distortion, i.e., $\boldsymbol{F}^{*} = \boldsymbol{R}^{*}\boldsymbol{U}^{*}$.

As mentioned earlier, from the initial state to the intermediate state of the crystal, dislocation occurs to induce the plastic deformation but lattice distortion does not occur. It can be reasonably assumed that the orientation of the slip system, described by the unit vectors $\boldsymbol{s}^{(\alpha)}$ along the slip direction and $\boldsymbol{m}^{(\alpha)}$ along the normal of the slip plane in the α slip system, remains during the plastic deformation, and only changes during the elastic deformation from the intermediate state to the current state of the crystal. It should be noted the elastic lattice distortion is usually small and negligible compared to the plastic deformation. Therefore, the rigid-body rotation is regarded as the main cause for the orientation change of the slip system. Under such a case with $\boldsymbol{F}^{*} = \boldsymbol{R}^{*}\boldsymbol{U}^{*} \approx \boldsymbol{R}^{*}$, by establishing the relationships between the vectors $\boldsymbol{s}^{(\alpha)}$ and $\boldsymbol{m}^{(\alpha)}$ in the current configuration and the unit vectors $\boldsymbol{s}_0{}^{(\alpha)}$ and $\boldsymbol{m}_0{}^{(\alpha)}$ in the initial configuration, the changes in the orientations of the slip system can be given as

$$\boldsymbol{s}^{(\alpha)} = \boldsymbol{R}^{*} \bullet \boldsymbol{s}_0{}^{(\alpha)} \tag{2}$$

$$\boldsymbol{m}^{(\alpha)} = \boldsymbol{m}_0{}^{(\alpha)} \bullet (\boldsymbol{R}^{*})^{T} \tag{3}$$

Further, the relationship between the plastic shear strain $\gamma^{(\alpha)}$ of the slip systems and the plastic deformation gradient $\boldsymbol{F}^{P}$ in the initial configuration can be expressed as

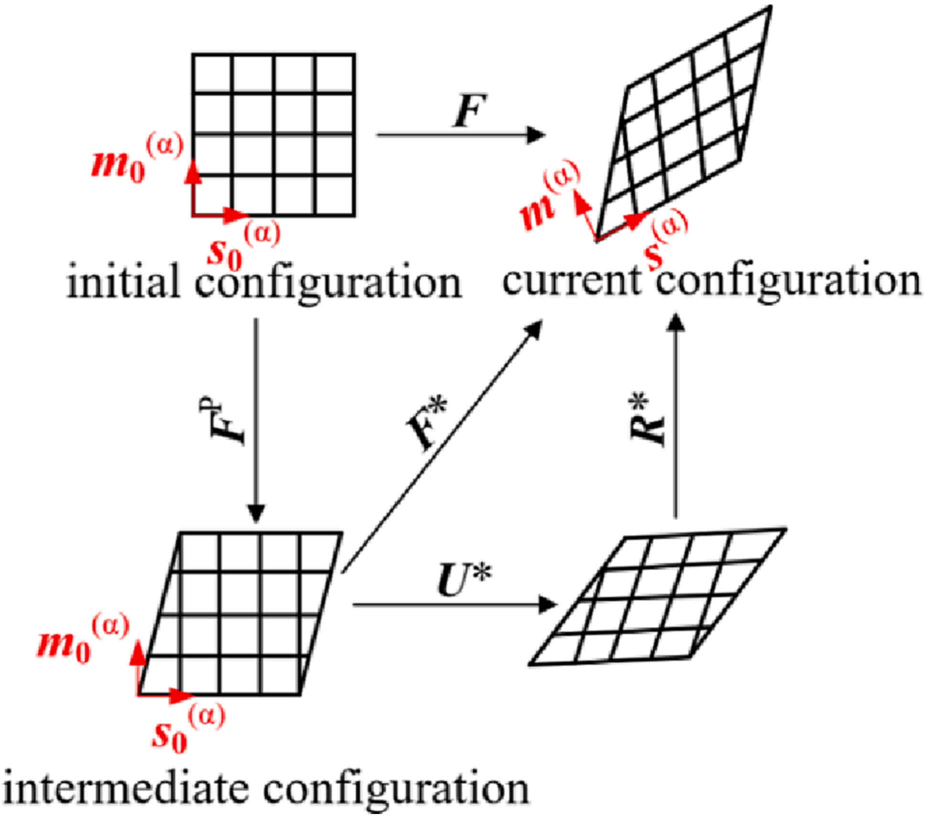

Fig. 1. Decomposition of total deformation gradient of crystal.

$$\boldsymbol{F}^{P}=\boldsymbol{I}+\sum_{\alpha=1}^{N}\gamma^{(\alpha)}\boldsymbol{s}_{0}{}^{(\alpha)}\ \boldsymbol{m}_{0}{}^{(\alpha)} \tag{4}$$

where $\boldsymbol{I}$ is the second order identical tensor, $\boldsymbol{N}$ is the total number of slip systems. The crystal structure of AgNP is a face-centered cubic crystal (FCC) with a total of 12 slip systems. $\boldsymbol{s}_0{}^{(\alpha)}\ \boldsymbol{m}_0{}^{(\alpha)}$ is the Schmid tensor.

By deriving the deformation gradient $\boldsymbol{F}$, the velocity gradient tensor $\boldsymbol{L}$ can be defined as

$$\boldsymbol{L}=\dot{\boldsymbol{F}}\boldsymbol{F}^{-1}=\frac{\partial\boldsymbol{F}}{\partial t}\boldsymbol{F}^{-1}=\dot{\boldsymbol{F}}^{*}\bullet\left(\boldsymbol{F}^{*}\right)^{-1}+\boldsymbol{F}^{*}\bullet\dot{\boldsymbol{F}}^{P}\bullet\left(\boldsymbol{F}^{P}\right)^{-1}\bullet\boldsymbol{F}^{*-1}=\boldsymbol{L}^{*}+\boldsymbol{L}^{P} \tag{5}$$

where $\boldsymbol{L}^{*}$ represents the elastic part of the velocity gradient tensor and $\boldsymbol{L}^{P}$ represents the plastic part of the velocity gradient tensor. Further, $\boldsymbol{L}$ can be decomposed into the deformation rate tensor $\boldsymbol{D}$ and the spin rate tensor $\boldsymbol{W}$ as

$$\boldsymbol{L}=\boldsymbol{D}+\boldsymbol{W} \tag{6}$$

$$\boldsymbol{D}=\frac{1}{2}\left(\boldsymbol{L}+\boldsymbol{L}^{T}\right)=\boldsymbol{D}^{*}+\boldsymbol{D}^{P} \tag{7}$$

$$\boldsymbol{W}=\frac{1}{2}\left(\boldsymbol{L}-\boldsymbol{L}^{T}\right)=\boldsymbol{W}^{*}+\boldsymbol{W}^{P} \tag{8}$$

where $\boldsymbol{D}^{*}$ and $\boldsymbol{D}^{P}$ are the elastic and plastic parts of the deformation rate tensor respectively, $\boldsymbol{W}^{*}$ and $\boldsymbol{W}^{P}$ are the elastic and plastic parts of the spin rate tensor respectively.

Based on the rate-dependent flow criterion [48,49], the shear strain rate $\dot{\gamma}^{(\alpha)}$ of the slip systems can be expressed by the resolved shear stress $\tau^{(\alpha)}$ and the critical resolved shear stress (CRSS) $g^{(\alpha)}$ as

$$\dot{\gamma}^{(\alpha)}=\dot{\gamma}_{0}\left|\frac{\tau^{(\alpha)}}{g^{(\alpha)}}\right|^{n}sign\left(\tau^{(\alpha)}\right) \tag{9}$$

where $\dot{\gamma}_0$ is the reference shear strain rate affecting the yield strength of the sintered AgNP, which is required to be further calibrated for sintered AgNP by fitting the numerical predictions to the experimental results under different loading conditions. $\boldsymbol{n}$ is the rate-dependent sensitivity coefficient. Note that $g^{(\alpha)}$ is associated with the stress for the initiation of a dislocation or for the onset of a dislocation motion. The two parameters $\tau^{(\alpha)}$ and $g^{(\alpha)}$ determine the plastic shear strain rate $\dot{\gamma}^{(\alpha)}$ of slip systems. It can be found that the active slip system and its shear strain rate can be uniquely determined by directly relating the shear strain rate to the shear stress of the slip system. However, when the shear stress is less than the critical shear stress of slip system, the plastic shear strain rate is much less than the reference shear rate. Under such conditions, the slip system can be considered as inactive.

It is well known that strain hardening is attributed to the interaction between dislocations [50]. Thus, the physical essence of strain hardening process of the crystal remains to be further revealed. In order to simplify the derivation and implementation of the proposed crystal plastic model, the strain hardening is described in Eq. (10) by the evolution of $g^{(\alpha)}$ according to the phenomenological hardening model in an incremental form of

$$\dot{g}^{(\alpha)}=\sum_{\beta}h_{\alpha\beta}\dot{\gamma}^{(\beta)} \tag{10}$$

where $h_{\alpha\beta}$ is the hardening modulus. When $\alpha=\beta$, $h_{\alpha\alpha}$ is regarded as the self-hardening modulus. When $\alpha\neq\beta$, $h_{\alpha\beta}$ is regarded as the latent hardening modulus. By following the references [18,51], $h_{\alpha\beta}$ and $h_{\alpha\alpha}$ are defined as

$$h_{\alpha\beta}=qh_{\alpha\alpha} \tag{11}$$

$$h_{\alpha\alpha}=h_{0}\,sech^{2}\left|\frac{h_{0}\gamma}{\tau_{s}-\tau_{0}}\right| \tag{12}$$

where q is the hardening ratio, the value of which in this paper is taken as 1.0. h_0 is the initial hardening modulus, τ_0 is the initial critical resolved shear stress, τ_s is the saturated flow stress, and γ is the cumulative plastic shear strains of all slip systems.

According to Hill and Rice [16], the elastic constitutive relationship of single crystals is described as

$$\widehat{\boldsymbol{\sigma}}^{*}=\boldsymbol{\psi}^{*}:\boldsymbol{D}^{*} \tag{13}$$

where $\boldsymbol{\psi}^{*}$ is the elastic modulus tensor. $\widehat{\boldsymbol{\sigma}}^{*}$ is the Jaumann derivative of the Cauchy stress tensor $\boldsymbol{\sigma}$ based on the intermediate configuration.

Based on the above analysis, the values of critical parameters deserve to be further investigated and calibrated for sintered AgNP subjected to different temperatures and strain rates, so that a reliable CP framework can be established to reveal the deformation mechanism and also shed light on the design of mesoscopic sintered structures of AgNP pastes.

3. Two-dimensional polycrystalline modeling

Polycrystalline is composed of a certain number of single crystals with different shapes and orientations. The polycrystalline properties are influenced by the single crystals and their interactions. Therefore, a polycrystalline FE model is the prerequisite for investigating the local plastic deformation of polycrystalline materials.

3.1. Polycrystalline FE model by Voronoi tessellation method

So far, the Voronoi tessellation method has been widely used to represent the mesoscopic structure of polycrystals [52–54]. By using the Python programming language, the polycrystalline FE model in ABAQUS based on the Voronoi tessellation method can be conveniently established. The SciPy package of Python is used to generate the Voronoi diagrams, and then the coordinates of vertices in the Voronoi diagrams are obtained. By importing the script file into ABAQUS, a polycrystal model is generated including a certain number of single crystals of different sizes and shapes. The established model is assigned with random orientations to each grain by efficiently creating a certain number of material parameters and section properties by Python at one time.

It is reported that AgNP powders are filled in a rectangular mold, and a rectangular plate with a size of 30 × 6 × 0.8 mm is obtained after sintering by applying auxiliary pressure to the sample using a pressure sensor [55]. In this paper, a three-dimensional polycrystalline model is considered to be simplified to a two-dimensional model to greatly improve the computational efficiency. As shown in Fig. 2, a representative area of 10 μm × 10 μm is established, in which 100 grains are randomly generated. Each polygon represents a grain and different colors represent different grain orientations. The model is discretized by four-node plane stress elements CPS4. The applied displacement and boundary conditions for the model area are also indicated in Fig. 2 to simulate the uniaxial tensile test on sintered AgNP.

3.2. Calibration of CPFEM parameters

The mesoscopic constitutive parameters of sintered AgNP for CPFEM are calibrated by comparing the uniaxial tensile tests and numerical simulations. The uniaxial stress–strain data is collected from the published works by Qian *et al.* [55]. For FCC crystals, three intrinsic moduli of elasticity (C_{11}, $C_{12,}$ and C_{44}) are critical to describing the elastic part of the stress–strain curve. This means that these elastic parameters can be determined when a good agreement is achieved between CPFEM predictions and experimental measurement for the elastic part of the stress–strain curve.

In this paper, the anisotropic elastic behavior of different grains in polycrystals is ignored during the parameter calibrations, while the plastic anisotropic behavior of the grains due to different orientations is significantly emphasized. Therefore, the initial values of the isotropic elastic parameters (C_{11}, C_{12} and C_{44}) for polycrystals are preliminarily determined by using Eqs. (14)-(16) and then continuously adjusted to fit the stiffness matrix at different temperatures and strain rates [55].

$$C_{11} = \frac{1-v}{(1+v)(1-2v)}E \tag{14}$$

$$C_{12} = \frac{v}{(1+v)(1-2v)}E \tag{15}$$

$$C_{44} = (C_{11} - C_{12})/2 \tag{16}$$

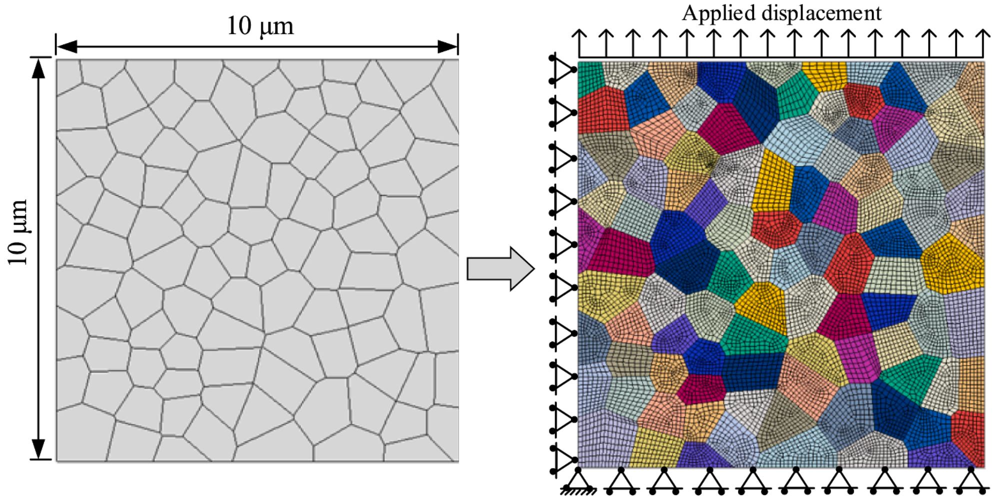

Fig. 2. Polycrystalline FE model with 100 grains: (a) Voronoi diagram; and (b) applied displacement and boundary conditions.

where E and v are elastic modulus and Poisson's ratio respectively.

In addition to the elastic parameters, other CP constitutive parameters are adjusted by the trial-and-error method [29,56,57] and finally determined by comparing the post-yielding stages of the CPFEM predictions and experimental curves. This method is also similar with the works by Jin *et al.* [28]. With the same remaining parameters, it is found that the hardening of the plastic stage of the material becomes more pronounced as h_0 and τ_s increase. However, both variables have no obvious effect on the yield strength of the curve. On the contrary, τ_0 determines the yield strength of the material, and the larger the value of τ_0, the larger the corresponding yield strength. Therefore, after determining the values of n and $\dot{\gamma}$, these three parameters (h_0, τ_s and τ_0) are mainly adjusted to simulate the plastic stage of the stress–strain curve. In this study, the rate-dependent sensitivity coefficient n is taken as 6.5, and the other parameter values are adjusted through iteration until the proposed CPFEM can accurately predict the experimental constitutive curve. CP parameters of sintered AgNP under different load conditions are finally listed in Table 1.

Based on the analysis above, the CP parameters are calibrated to best reproduce the stress–strain curves of sintered AgNP under uniaxial tension at different strain rates ($10^{-5}\ \mathrm{s}^{-1}$, $10^{-4}\ \mathrm{s}^{-1}$, $10^{-3}\ \mathrm{s}^{-1}$) and temperatures (-40 °C, 0 °C, 25 °C, 60 °C). The predicted results by the proposed CPFEM are shown in Fig. 3, which are in good agreement with the reported experimental results. The good agreement indicates that the proposed CPFEM with the calibrated parameters can satisfactorily predict the stress–strain responses of sintered AgNP polycrystalline materials. Further investigations can be reliably performed by this calibrated CPFEM to unveil the effects of mesoscopic properties on the macroscopic deformation and failure behavior.

4. Results and discussions

4.1. Von Mises stress contours at different temperatures and strain rates

As one of the major advantages of CPFEM, the heterogeneous deformation can be predicted by taking account of the anisotropic elastic and plastic properties at the *meso*-scales. With the calibrated mesoscopic parameters, the good agreement between predicted and measured uniaxial stress–strain responses confirms that the proposed CPFEM is capable of reasonably revealing the macroscopic constitutive characteristics of sintered AgNP at different temperatures and strain rates. Thus, high credibility is believed in the predicted heterogeneous deformation for the polycrystalline FE model produced by the Voronoi tessellation method. For objective comparisons with the *meso*-scale polycrystalline FE model with the same grain sizes and shapes, the contours of von Mises stress for sintered AgNP at the strain of 1.2 % under different loading conditions are illustrated in Fig. 4.

Based on the von Mises contour comparisons, it is observed that CPFEM can reasonably simulate the deformation characteristics of grains at the *meso*-scale. The deformation of each polycrystalline is affected by the internal grain orientation. According to Fig. 4(a1) and (a4), the stress tends to concentrate in the polycrystal at low temperature (-40 °C), while the stress is smeared on the polycrystalline at high temperature (60 °C). This trend stands for the results subjected to all three strain rates. Furthermore, comparing the contours in the first and third rows in Fig. 4, it is found that the stress distribution is more uniform under a higher strain rate ($10^{-3}\ \mathrm{s}^{-1}$). It is speculated that the mesoscopic deformation develops more actively at lower strain rates and higher temperatures to reflect the influences of grain characteristics. It can be inferred that some areas in the polycrystal are subject to higher stresses, which are usually the positions where fractures occur in sintered AgNP materials [58]. Stress concentration can lead to the further propagation of cracks and ultimately a significant degradation in the mechanical properties of the sintered AgNP material.

To explain the von Mises stress contour from a mesoscopic perspective, the distributions of CRSS and $\tau^{(\alpha)}$ of the $\{1\,1\,1\} < 0\text{–}11 >$ slip system at -40 °C and strain rate of $10^{-5}\ \mathrm{s}^{-1}$ are given in Fig. 5. At the *meso*-scale, it is the shear stress along the slip plane that drives the dislocation motion. The slip process is initiated only when the shear stress exceeds a certain critical value. From the simulation results in Fig. 5, it can be seen that the grain orientations and the magnitude of CRSS jointly determine the onset and activity of the $\{1\,1\,1\} < 0\text{–}11 >$ slip system during plastic deformation. Thus, when the shear stress of the slip system reaches the CRSS value, dislocations start to move along the slip plane within the crystal, leading to a decrease in stress in this region. However, the interaction of dislocations impedes its further motion, leading to a high stress region in polycrystals. Therefore, it can be speculated that the active states of all slip

Table 1
CP parameters of sintered AgNP under different load conditions.

Strain rate	Temperature	C_{11}	C_{12}	C_{44}	n	$\dot{\gamma}_0$	h_0	τ_s	τ_0
s^{-1}	°C	MPa	MPa	MPa	–	s^{-1}	MPa	MPa	MPa
10^{-5}	−40	10,166	4356	2904	6.5	0.0012	100.0	28.0	25.0
	0	8007	3432	2000	6.5	0.0012	95.0	25.0	22.5
	25	6008	2575	1550	6.5	0.0012	92.5	20.0	16.0
	60	3280	1406	937	6.5	0.0012	90.0	19.5	11.0
10^{-4}	−40	11,846	4500	3000	6.5	0.012	102.0	28.5	25.6
	0	8963	3841	2350	6.5	0.012	100.5	26.0	24.5
	25	8108	3475	2000	6.5	0.012	96.0	23.5	21.5
	60	7950	3407	1534	6.5	0.012	95.0	20.5	17.5
10^{-3}	−40	10,800	4628	3085	6.5	0.12	105.0	30.5	28.0
	0	11,497	4927	2850	6.5	0.12	103.5	30.0	27.5
	25	7696	3298	1699	6.5	0.12	102.0	29.5	27.0
	60	6841	2932	1454	6.5	0.12	100.0	26.5	24.0

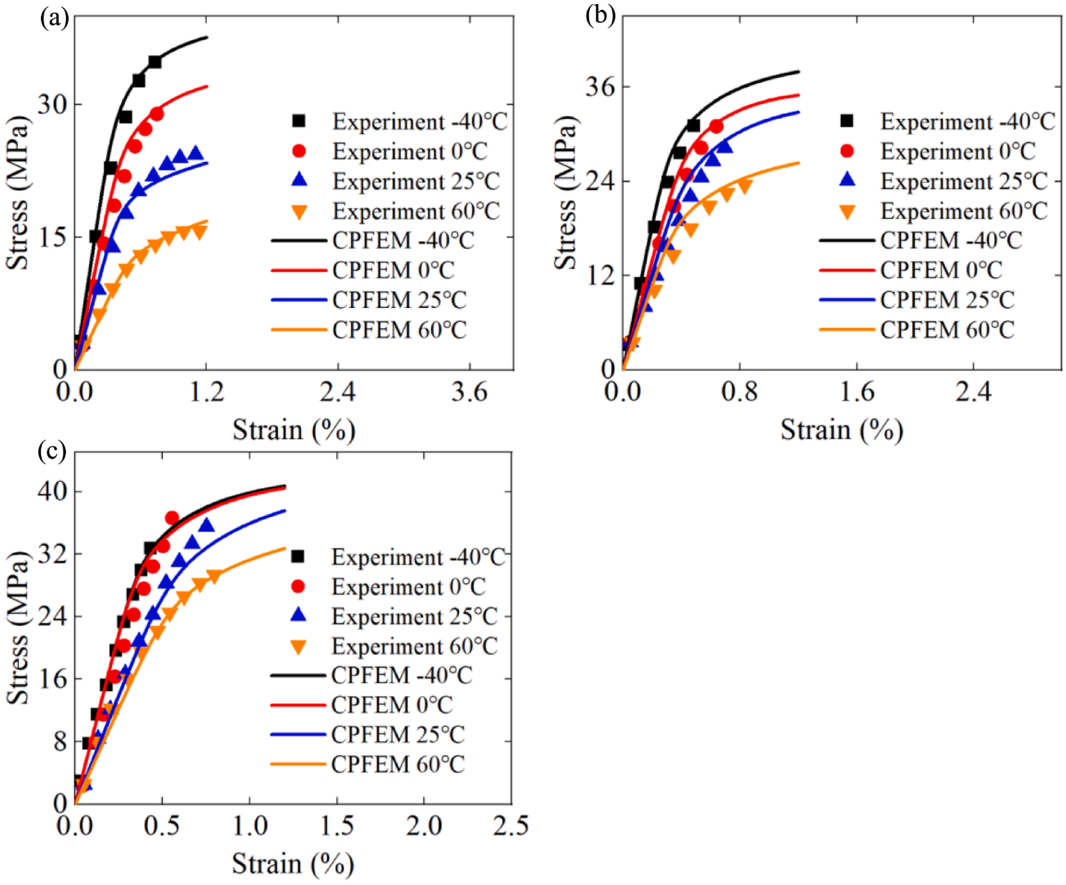

Fig. 3. Result comparisons of experiments and CPFEM simulations for the stress–strain curves at different temperatures and strain rates:(a) 10^{-5} s^{-1}; (b) 10^{-4} s^{-1}; and (c) 10^{-3} s^{-1}.

systems within the crystal under macroscopic loading jointly determine the distribution of stresses within the polycrystal.

4.2. Effect of different number of grains in RVE model

Both the initial orientation and the grain size in the polycrystalline FE model have significant effects on the macroscopic stress and strain of polycrystals [59]. Considering that the grains with different sizes will be formed during the sintering process, the RVE models with 25, 50, 75 and 100 grains are further created to consider different grain sizes, as shown in Fig. 6. For different models, 15 independent groups of random grain orientations are assigned. The simulations subjected to uniaxial tensile stress for the polycrystalline model are carried out at −40 °C and a strain rate of 10^{-4} s^{-1} until the strain of 1.2 %.

The simulation results in Fig. 7 show that the random orientation of the grains has the most obvious effect on the macroscopic stress and strain of the anisotropic material when the polycrystalline FE model contains the least grain number (i.e. 25 grains), and the difference of macroscopic stress in the post-yielding stage between different groups of random orientations can reach the maximum value of 5.5 MPa at the strain of 1.2 %. As shown in Fig. 7(e), the effect of random grain orientation on the macroscopic stress–strain response of the polycrystalline FE model progressively decreases with the further increase of the number of grains during the crystal deformation. When the grain number is 100, the difference between the macroscopic stress–strain curves of the various groups seems to be stabilized and does not further decrease significantly even a greater number of grains are adopted as shown in the inset of Fig. 7 (e). As a balance between computational cost and prediction accuracy, the grain number for such an area of 10 μm × 10 μm of sintered AgNP is therefore suggested to be 100 for calibrating the CPFEM parameters by using a polycrystalline model based on the Voronoi tessellation method. With statistical significance, this crystal scheme can minimize the effect of the randomness of initial grain orientation in the polycrystalline FE model on the macroscopic stress–strain responses of the polycrystals.

Additionally, a set of random orientations is selected for each polycrystalline model and from the mesoscopic perspective, the maximum, minimum, and mean values of the average resolved shear stresses are summarized in Fig. 8 for all slip systems of each grain in RVE models containing 25 and 100 grains, respectively. It can be seen that in the model containing 25 grains, the shear stress range of most grains is larger than that of the model with 100 grains. Furthermore, the percentage of grains with different shear stress ranges are counted in the histogram in Fig. 8. These show the percentage of grains with smaller shear stress ranges is higher as the number of

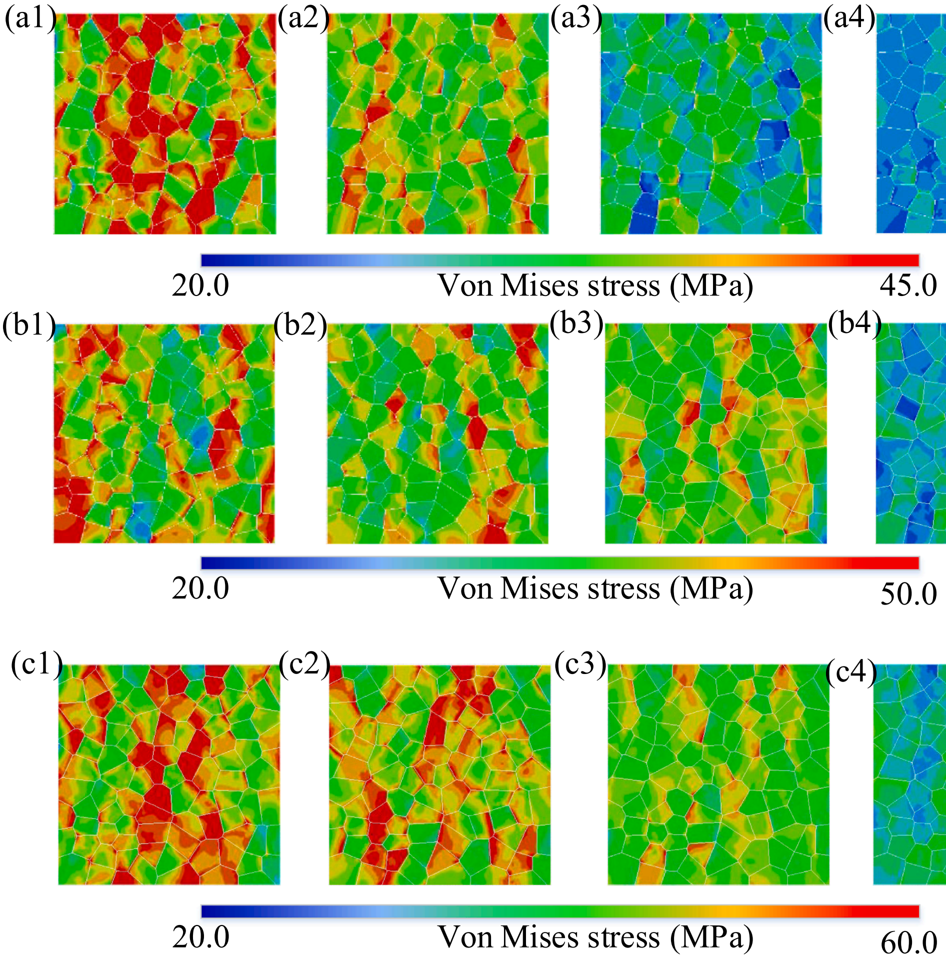

Fig. 4. Von Mises stress contours of sintered AgNP at the strain of 1.2 % under different loading conditions: (a–c) strain rates of 10^{-5} s^{-1}, 10^{-4} s^{-1}, and 10^{-3} s^{-1}; and (1–4) the temperature of −40 °C, 0 °C, 25 °C, and 60 °C, respectively.

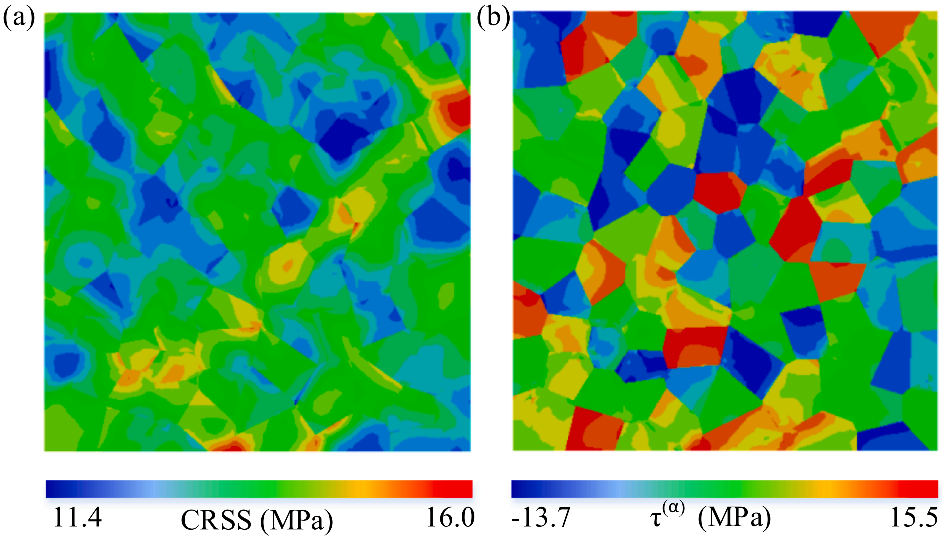

Fig. 5. Distributions of CRSS and $\tau^{(\alpha)}$ of the {1 1 1} < 0–11 > slip system for sintered AgNP at −40 °C and strain rate of 10^{-5} s^{-1}: (a) CRSS; and (b) $\tau^{(\alpha)}$.

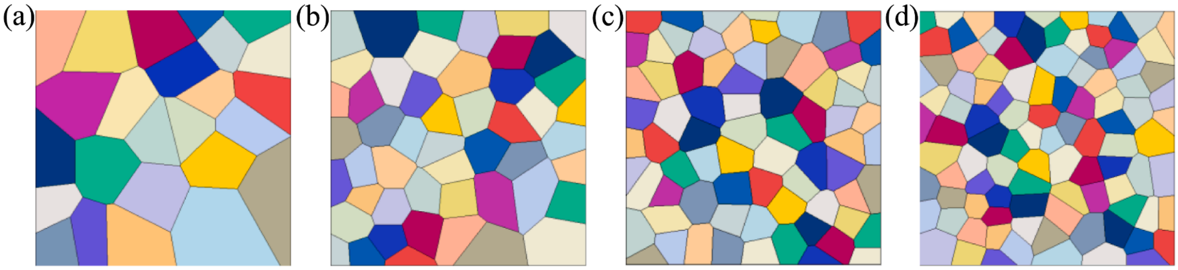

Fig. 6. Polycrystalline FE model with different numbers of grains: (a) 25 grains; (b) 50 grains; (c) 75 grains; and (d) 100 grains.

grains increases. This statistical result convinces the conclusions regarding the grain number for calibrating the CPFEM parameters by using a polycrystalline model of sintered AgNP. That is, the mechanical properties of the polycrystalline model containing 100 grains are believed to be predicted at a sufficiently high simulation accuracy and affordable computational efficiency for the area of 10 μm × 10 μm of sintered AgNP. This also explains why the range of macroscopic stress–strain curves is the smallest for a different group of grain orientations of the FE model with 100 grains.

4.3. *Effect of initial grain orientation*

It is evident in the previous analysis that stress and strain inhomogeneities exhibit within the polycrystal structure. Regarding crystal features, the initial grain orientation is important to deeply understand the mechanical properties of sintered AgNP. Fig. 9 shows the effect of different grain orientations on the overall average stress and strain in the polycrystalline based on the stress and strain values of sintered AgNP in the tensile direction at −40 °C and a strain rate of 10^{-4} s^{-1}. When the macroscopic deformation of the polycrystal reaches 1.2 %, the stress and strain of the individual grains are provided in Fig. 10. It is demonstrated that the macroscopic stress of polycrystals is the averaging result of multiple anisotropic grains.

To explore the underlying mechanism of grain orientation to influence the stress distribution, the six grains with the higher stress or strain values as highlighted in Fig. 9 are further examined. It is worth noting that Euler angles are listed in Table 2 to represent the crystal orientation of these six grains of interest. Their corresponding crystal orientations are shown in Fig. 9. It can be seen that the arrangement of the six grains with different orientations with respect to the reference coordinate system considerably differs, which leads to the complex distributions of stresses and strains within these six grains in Fig. 9. It can be seen that the grains 17, 76 and 85 have higher stresses at the grain boundaries, particularly at the intersections of the grain boundaries.

This is due to the mismatch of mechanical properties of different grains and the inhomogeneous constraints among grains. It is well known that the CP theory is based on Taylor model [14], which assumes that the deformation coordination conditions are satisfied between the grains within the polycrystal, and destroys the stress equilibrium conditions at the grain boundaries. Therefore, under external loading, the grains that are likely to slip are subjected to greater deformation as the hardening rate decreases, resulting in relatively lower stresses, while the requirement for deformation coordination causes some grains that are difficult to slip to be subjected to greater loads, resulting in a larger difference in stress between the grain boundary and the grain interior. It is anticipated that the failure of sintered AgNP is likely to start from the grain boundary under the axial tension, i.e. intergranular fracture. As described by Benedetti *et al.* [60], the grain boundary failure usually occur due to the accumulation of defects under loading. Regarding the strain distribution, the strain in grain 56 becomes sharply larger close to the grain boundary. In contrast, the strain inside grains 37 and 57 is observed to become progressively smaller along the center of the grain to the edge of the grain boundary. These observations consistently indicate that the grain orientation has a significant effect on the stress and strain.

With greatly different orientations, the six grains show different stress–strain responses during the uniaxial tensile deformation in Fig. 11. For the grains 17, 76, and 85 with Euler angles (51°, 78°, 80°), (23°, 9°, 16°) and (37°, 55°, 19°), the stress values are 51.56 MPa, 48.43 MPa, and 48.97 MPa, respectively, which are approximately 1.27–1.35 times the average polycrystal stress. The corresponding strain values are slightly lower than the macroscopic polycrystal strain. This indicates that these three grains with higher stress contribute more strength and slip resistance compared to the other grains. For the grains 37, 56, and 57 with Euler angles (6°, 13°, 87°), (62°, 29°, 21°), and (15°, 22°, 72°), the strain values are much higher than the macroscopic strain, and the stress values are slightly lower than the macroscopic stress, which leads to the conclusion that these grains with higher strain values contribute more local deformation because of active slip system. This also confirms that the grains in lower stressing regions reach the critical resolved stress earlier and start to slip first, while the grains with higher slip resistance slip later. It can therefore be inferred that the orientation distribution in the polycrystals determines the *meso*-scale mechanical behavior. The mesoscopic characteristics of different grains within the polycrystal can be visualized by using CP constitutive model simulations. This finding is consistent with the results found by Jin *et al.* [28] that “soft” and “hard” grains in polycrystals can be distinguished based on the stress and strain results of different grains obtained from the CP model, where the “soft grain” is easier to slip than the “hard grain”. Thus, the inhomogeneity of stress and strain in the grains within the polycrystal under tension is severe and the overall average values of stress and strain in the polycrystal are attributed to the degree of inhomogeneous deformation.

According to Schmid’s law, the relative position between the slip system and tension direction determines the degree of activation of the slip system [15]. It is well known that grains are more likely to slip with a larger Schmid factor (SF). The comparisons between

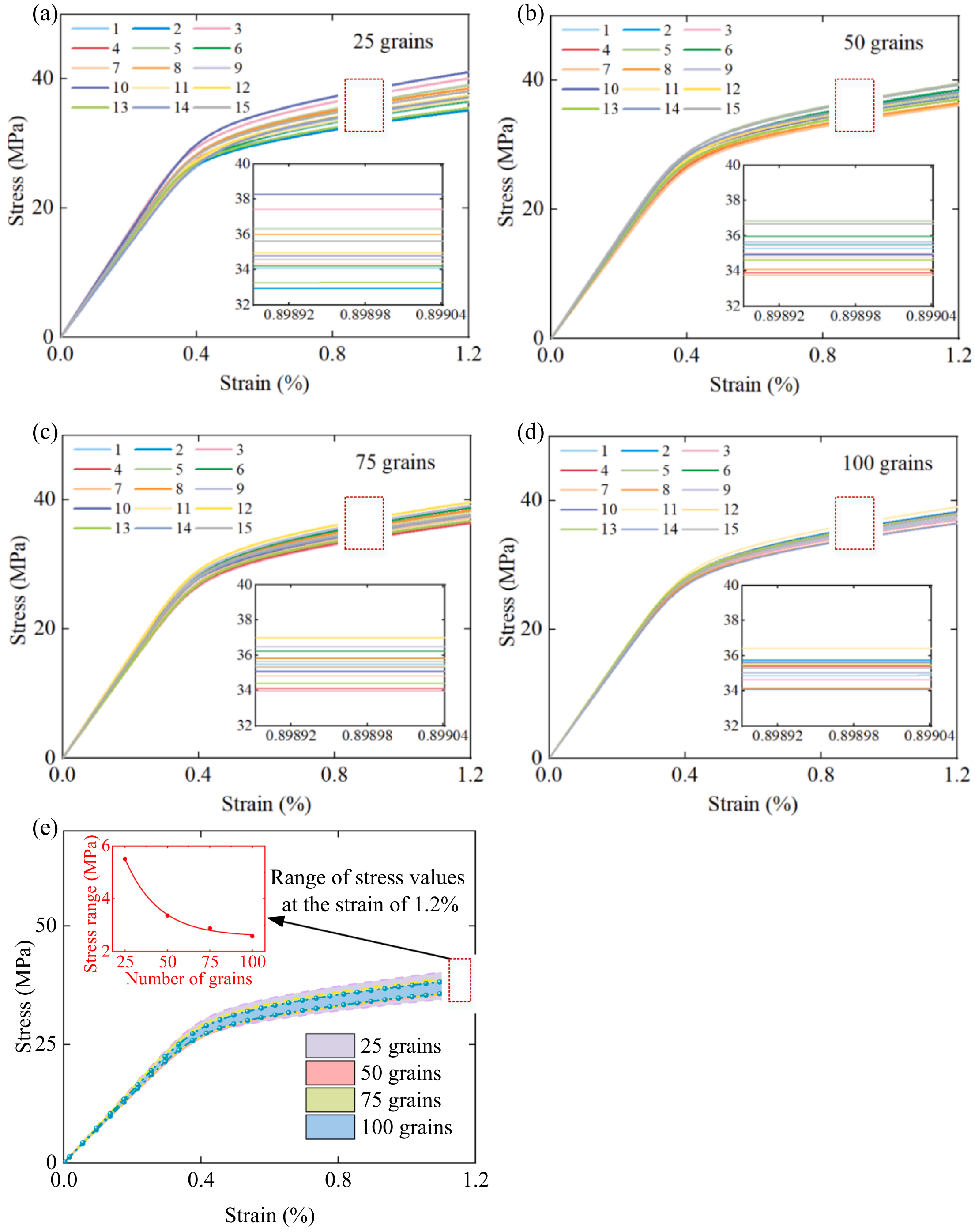

Fig. 7. Stress–strain curves for RVE models containing different number of grains: (a) 25 grains;(b) 50 grains; (c) 75 grains; (d) 100 grains; and (e) stress–strain curves in comparison.

the distribution of the average SF for all slip systems and the strain distribution of the polycrystals are shown in Fig. 12. It is obvious that the crystal deformation is closely related to SF which is found to be higher in the high-strain area. which links to the conclusion above that there are more active slip systems in the grains in the high-strain area. In addition, Fig. 13 shows the evolution process of the maximum value of the SF for all slip systems of the six grains due to the crystal rotation during crystal deformation. The SF of grains 17, 85 and 37 at 1.2 % strain is less than the initial SF, so the orientation of these three grains changes in the direction that is more unfavorable to the activity of the slip systems during tension. In contrast, with a greater SF at a strain of 1.2 %, grain 76 has a more favorable grain orientation. The final orientations of grains 56 and 57 tend to be similar to the initial orientation after continuous

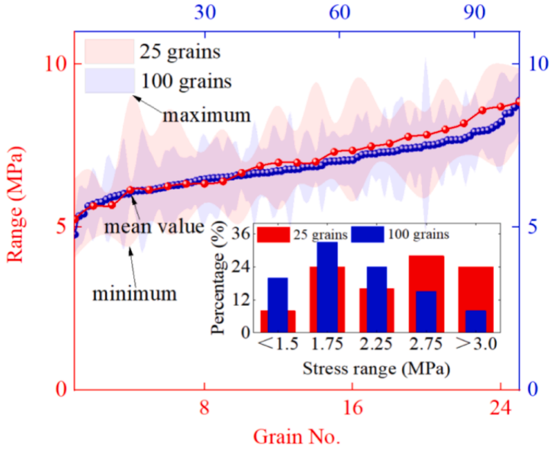

Fig. 8. Maximum, minimum and mean value of average resolved shear stresses of each grain in RVE models containing 25 grains or 100 grains.

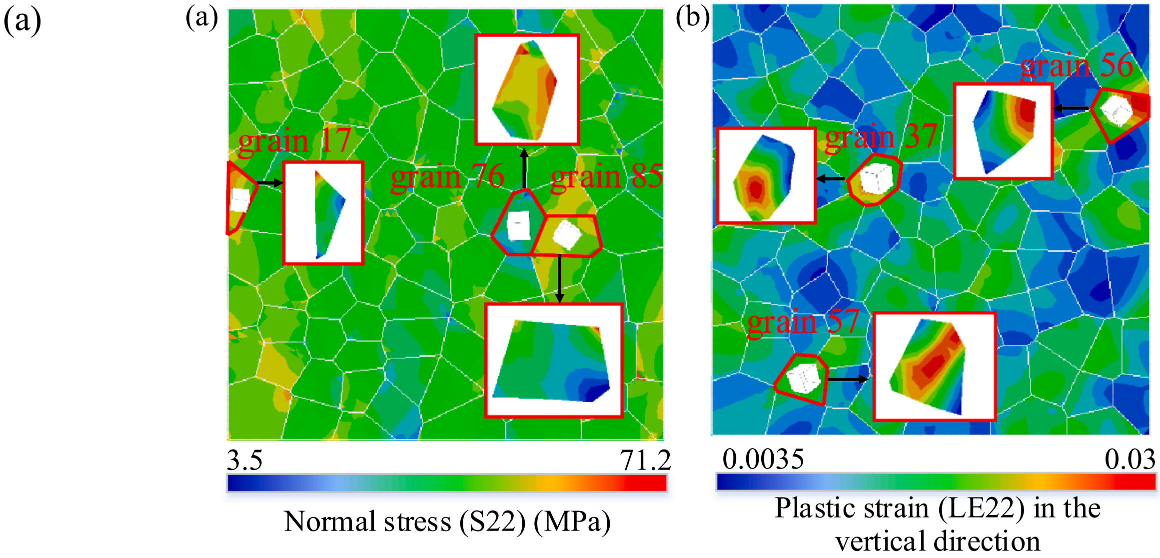

Fig. 9. Stress and strain contours in the polycrystal structure at −40 °C and the strain rate of 10^{-4} s^{-1}: (a) normal stress (S22); and (b) plastic strain (LE22) in the vertical direction.

rotations. These verify this conclusion that the grain rotation is closely related to the grain orientation [61], leading to substantially different degrees of deformation and stress distribution within the polycrystal.

The cumulative plastic shear strain distribution resulting from the slip systems of the polycrystals during uniaxial tension is shown in Fig. 14(a). Similarly, Fig. 14(b) shows the cumulative plastic shear strain curves for these six grains highlighted in Fig. 9. It can be seen that the overall activity of the slip systems of crystals with various initial orientations is greatly different. It is widely known that there are 12 slip systems for FCC crystals. As shown in Fig. 15, the cumulative shear strain of each slip system is extracted for "soft grain" 56 and "hard grain" 85 as examples, respectively. For grain 56, it can be seen from Fig. 15(a) that there are five slip systems with larger shear strains while the shear strains of the other seven slip systems are almost zero during tension. This can be predicted that five slip systems of grain 56 are significantly activated during the tensile deformation. Particularly, the shear strain in $\{11\text{–}1\}$ $\langle -1\,1\,0\rangle$ slip system tends to increase rapidly with the increase of the deformation, reaching around 0.025, which is about 30 times the shear strain of the $\{-1\,1\,1\}$ $\langle 1\,1\,0\rangle$ slip system. This suggests that the $\{11\text{–}1\}$ $\langle -1\,1\,0\rangle$ slip system is the most active compared to the other slip systems of grain 56, and therefore, this slip system provides more plastic strain during crystal deformation. Similarly, Fig. 15(b) shows the shear strains of the different slip systems within the "hard grain" 85. It is shown that there are four slip systems constantly generating shear slip, but the shear strain in the most active $\{-1\,1\,1\} < 0\text{–}11 >$ system is quite small compared to grain 56. Combining the distribution of the SF of slip systems varies considerably between different grains and the shear deformation of the activated slip system within a grain is also different due to the grain orientation. Therefore, it can be concluded that the slip systems and the tension direction of grain 56 are in "soft orientation", which makes it easier to slip, while the slip systems and the tension direction are in "hard

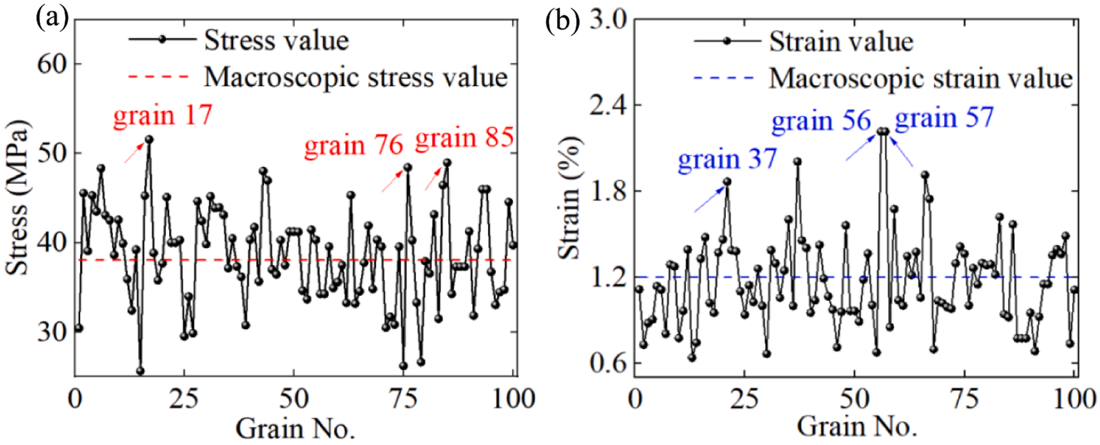

Fig. 10. Stress and strain values of individual grains at −40 °C and the strain rate of 10^{-4} s^{-1}: (a) normal stress (S22); and (b) plastic strain (LE22) in the vertical direction.

Table 2
Euler angles and their orientations of the six grains with higher stress or strain values.

Grain No.	Euler angles
17	(51°, 78°, 80°)
76	(23°, 9°, 16°)
85	(37°, 55°, 19°)
37	(6°, 13°, 87°)
56	(62°, 29°, 21°)
57	(15°, 22°, 72°)

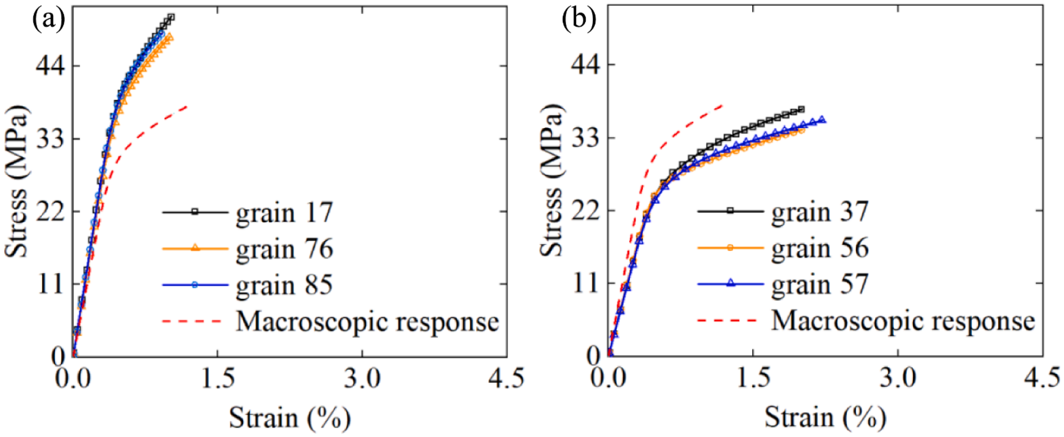

Fig. 11. Stress–strain curves of the six grains: (a) grain17, grain76, and grain85; (b) grain37, grain56, and grain57.

orientation" of grain 85. Moreover, another conclusion can be drawn that the degree of plastic shear deformation in individual grains and different grain orientations lead to stress/strain concentration in polycrystals.

5. Conclusions and remarks

The deformation behavior of sintered AgNP is closely related to the *meso*-scale polycrystalline structure. CPFEM simulations of the sintered AgNP material under uniaxial tension at different strain rates and temperatures are carried out to establish the relationship between the *meso*- and macro-scale deformation response. The uniaxial stress–strain curve predicted by CPFEM is consistent with the experimental results, which confirms the reasonable calibration of CP parameters of sintered AgNP polycrystalline materials. More

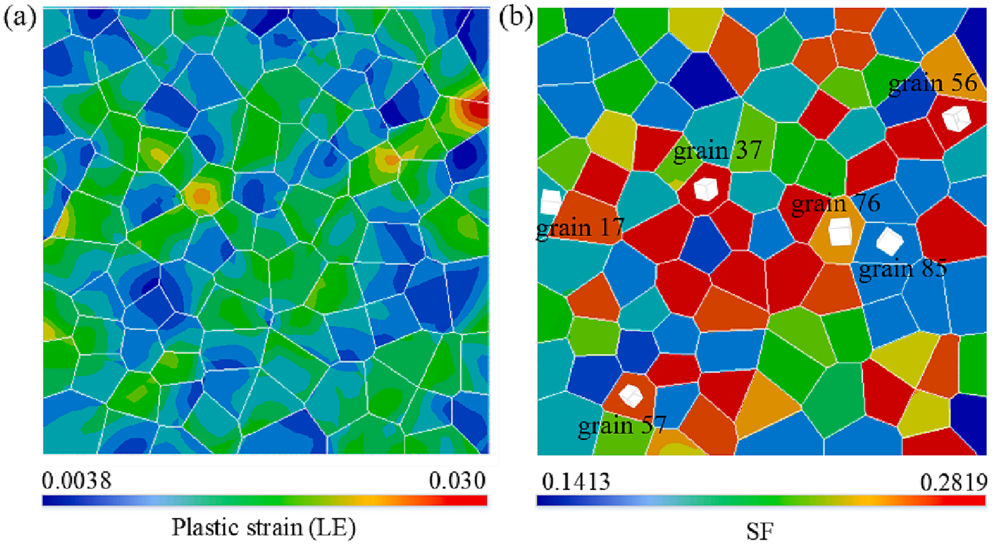

Fig. 12. Comparison between the strain contour and the average SF distribution diagram: (a) plastic strain (LE), and (b) average SF.

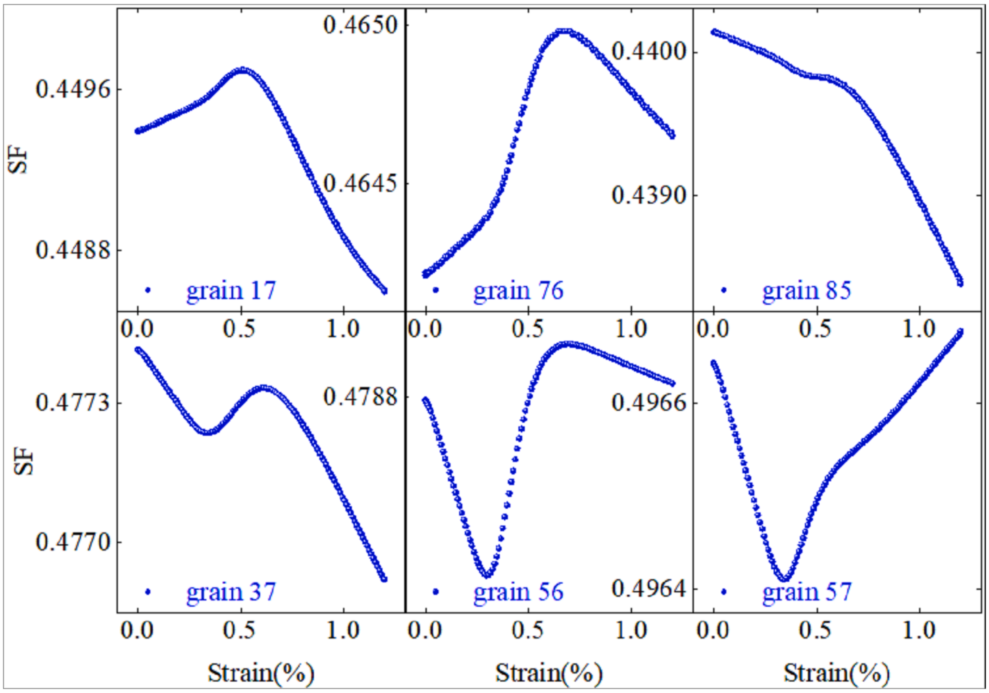

Fig. 13. Maximum value of the SF for all slip systems of the six grains.

importantly, the *meso*-scale distributions of von Mises stress and critical resolved shear stress are confidently illustrated. To achieve objective simulations independent of grain characteristics, the effects of the number of grains on the mechanical behavior of sintered AgNP are revealed with random grain orientations.

It is found that the difference of the macroscopic mechanical response of sintered AgNP materials under different orientations weakens with the increase of the number of grains in the RVE model. After examining the effect of initial grain orientation, it is found that there are significant differences in the activity of the slip systems of crystals with various orientations. In addition, the stress and strain at the grain boundary change sharply due to different crystal orientations, which suggests that the failure of sintered AgNP initiates from the grain boundary with lower slip resistance under the uniaxial tension condition.

It is worth noting that porous structures formed during the sintering process of AgNPs has a significant impact on the macroscopic mechanical properties of sintered silver. As the *meso*-scale structure is not available with sufficient details in the literature, the porous

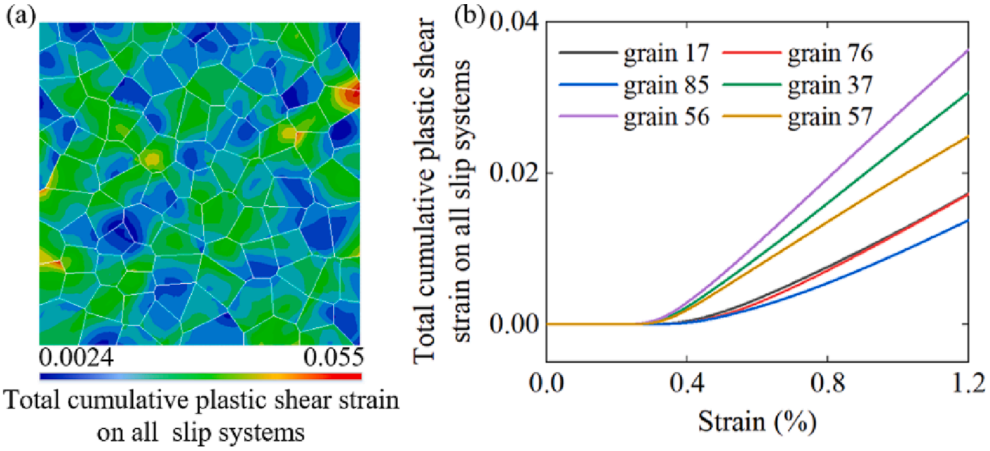

Fig. 14. Total cumulative plastic shear strain on all slip systems: (a) total cumulative shear strain distribution; and (b) total cumulative shear strain curves of the six grains.

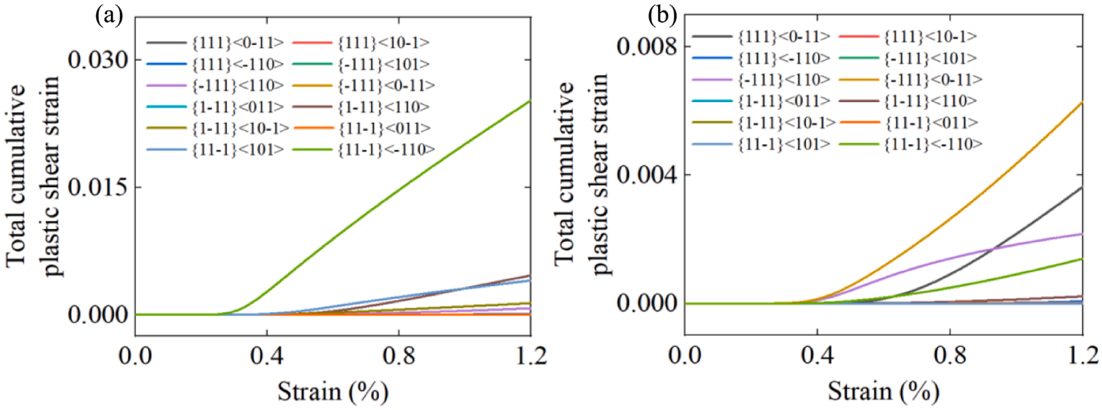

Fig. 15. Total cumulative shear strain γ in the slip systems under the uniaxial tensile deformation: (a) grain56; and (b) grain 85.

structures of sintered AgNP are not considered in the polycrystalline model of this paper. Therefore, the random porous structure can be embedded into the polycrystalline model by aligning numerical simulations and experimental observations in future studies. In addition, the adopted rate-dependent flow criterion in this paper has limitations to explicitly reflect the influence of microscopic mechanisms on the deformation behavior of crystalline materials. Since dislocation motion is the main mechanism to cause plastic deformation in crystalline materials, further studies to establish the relationship among shear strain rate, strain hardening and dislocation density are highly expected. Moreover, considering that the damage accumulation is closely related to the fatigue life of packaging structures under service conditions, the cumulative strain due to the activity of slip systems at the mesoscopic scale as predicted by the proposed CPFEM could be used as the indicator of the damage model to quantify the damage evolution of the sintered AgNP materials, providing an important insight into the design of particle morphology in the AgNP paste after the tunable sintering process. This means that the inhomogeneities of stress and strain distribution caused by crystal features of grain size and orientation can be predicted and thus designed based on the proposed CPFEM methodology and calibrated parameters in the present study.

CRediT authorship contribution statement

Xu Long: Validation, Supervision, Software, Methodology, Funding acquisition, Data curation, Conceptualization, Writing - original draft, Writing - review & editing. **Kainan Chonga:** Software, Investigation, Formal analysis, Data curation, Validation, Writing - original draft. **Yutai Su:** Writing – review & editing, Methodology, Conceptualization. **Leiming Du:** Writing – review & editing, Software, Conceptualization. **Guoqi Zhang:** Methodology, Conceptualization, Writing - review & editing.

Declaration of Competing Interest

The authors declare that they have no known competing financial interests or personal relationships that could have appeared to influence the work reported in this paper.

Data availability

Data will be made available on request.

Acknowledgement

This work was supported by the National Natural Science Foundation of China (No. 52175148), the Natural Science Foundation of Shaanxi Province (No. 2021KW-25), the National Key Laboratory Foundation 2022-JCJQ-LB-006 (No. 6142411232212), and Regional Collaboration Project of Shanxi Province (No.2022104041101122).

References

[1] Anand L. Constitutive equations for hot-working of metals. Int J Plast 1985;1(3):213–31.
[2] Bai N, Chen X, Gao H. Simulation of uniaxial tensile properties for lead-free solders with modified Anand model. Mater Des 2009;30(1):122–8.
[3] Lall P, Zhang D, Yadav V, Locker D. High strain rate constitutive behavior of SAC105 and SAC305 leadfree solder during operation at high temperature. Microelectron Reliab 2016;62:4–17.
[4] McDowell D.L, Miller M.P, Brooks D.C, *A unified creep-plasticity theory for solder alloys.* ASTM Special Technical Publication, 1994. **1153**: p. 42-42.
[5] Long X, He X, Yao Y. An improved unified creep-plasticity model for SnAgCu solder under a wide range of strain rates. J Mater Sci 2017;52(10):6120–37.
[6] Long X, Guo Y, Liu Y.C, Su Y.T, Siow K.S, Chen C.C, *A new unified creep-plasticity constitutive model coupled with damage for viscoplastic materials subjected to fatigue loading.* Fatigue & Fracture of Engineering Materials & Structures. (accepted).
[7] Chen X, Chen G, Sakane M. Prediction of stress-strain relationship with an improved Anand constitutive model for lead-free solder Sn-3.5 Ag. IEEE Trans Compon Packag Technol 2005;28(1):111–6.
[8] Wang F, Keer LM, Vaynman S, Wen SM. Constitutive model and numerical analysis for high lead solders. IEEE Trans Compon Packag Technol 2004;27(4):718–23.
[9] Long X, Guo Y, Su YT, Siow KS, Chen CT. Constitutive, creep, and fatigue behavior of sintered Ag for finite element simulation of mechanical reliability: a critical review. J Mater Sci Mater Electron 2022:1–17.
[10] Tasan CC, Hoefnagels JP, Diehl M, Yan DS, Roters F, Raabe D. Strain localization and damage in dual phase steels investigated by coupled in-situ deformation experiments and crystal plasticity simulations. Int J Plast 2014;63:198–210.
[11] Zener C, Hollomon JH. Problems in non-elastic deformation of metals. J Appl Phys 1946;17(2):69–82.
[12] Huang Y.G, *A user-material subroutine incroporating single crystal plasticity in the ABAQUS finite element program*. 1991, Harvard University, Cambridge, MA: Mechanical Report 178, Division of Applied Sciences.
[13] Orowan E. Zur kristallplastizität. *II* Zeitschrift Für Physik 1934;89(9):614–33.
[14] Taylor GI. Plastic strain in metals. J Inst Metals 1938;62:307–24.
[15] Read W.T, *Plasticity of crystals by E. Schmid and W. Boas.* Acta Crystallographica, 1951. **4**(4): p. 384-384.
[16] Hill R, Rice JR. Constitutive analysis of elastic-plastic crystals at arbitrary strain. J Mech Phys Solids 1972;20(6):401–13.
[17] Asaro RJ, Rice JR. Strain localization in ductile single crystals. J Mech Phys Solids 1977;25(5):309–38.
[18] Peirce D, Asaro RJ, Needleman A. An analysis of nonuniform and localized deformation in ductile single crystals. Acta Metall 1982;30(6):1087–119.
[19] Havner KS, Baker GS, Vause RF. Theoretical latent hardening in crystals—I. General equations for tension and compression with application to fcc crystals in tension. J Mech Phys Solids 1979;27(1):33–50.
[20] Peirce D, Asaro RJ, Needleman A. Material rate dependence and localized deformation in crystalline solids. Acta Metall 1983;31(12):1951–76.
[21] Roters F, *Advanced material models for the crystal plasticity finite element method: development of a general CPFEM framework*. 2011, RWTH Aachen University: Habilitation Thesis.
[22] Jiang MY, Fan ZX, Kruch S, Devincre B. Grain size effect of FCC polycrystal: a new CPFEM approach based on surface geometrically necessary dislocations. Int J Plast 2022:103181.
[23] Dindarlou S, Castelluccio GM. Substructure-sensitive crystal plasticity with material-invariant parameters. Int J Plast 2022;155:103306.
[24] Wang J, Zhou C.Z. *A meso-scale fretting fatigue simulation method based on submodelling technique.* in *ASME International Mechanical Engineering Congress and Exposition.* 2021. American Society of Mechanical Engineers.
[25] Sonawane D, Kumar P. Role of grain boundary sliding in structural integrity of Cu-filled through Si via during isothermal annealing. J Electron Mater 2021;50(3):767–78.
[26] Amelirad O, Assempour A. Coupled continuum damage mechanics and crystal plasticity model and its application in damage evolution in polycrystalline aggregates. Engng Comput 2021:1–15.
[27] Sasaki T, Yanase A, Okumura D, Kariya Y, Koganemaru M, Ikeda T. Measurements and FEM analyses of strain distribution in small Sn specimens with few crystal grains. Mater Trans 2019;60(6):868–75.
[28] Jin JY, Mei YH, Chen G, Chen X, Lu GQ. Modeling of intergranular mechanical fatigue of a sintered nanosilver die attachment for power electronics. IEEE Trans Compon Packag Manuf Technol 2020;10(6):982–9.
[29] Xie MW, Chen G, Yang J, Xu WL. Temperature-and rate-dependent deformation behaviors of SAC305 solder using crystal plasticity model. Mech Mater 2021;157:103834.
[30] Xie MW, Chen G, Yu JT, Wu YT, Liu X, Yang J, et al. A dual-phase crystal plasticity finite-element method for modeling the uniaxial deformation behaviors of thermally aged SAC305 solder. Int J Plast 2022:103342.
[31] Zhang Z, Liu S, Ma K, Shi TL, Qian ZF, Liang K, et al. A thermomechanical constitutive model for investigating the fatigue behavior of Sn-rich solder under thermal cycle loading. Fatigue Fract Engng Mater Struct 2022;45(7):1953–68.
[32] Xu YL, Xian JW, Stoyanov S, Bailey C, Coyle RJ, Gourlay CM, et al. A multi-scale approach to microstructure-sensitive thermal fatigue in solder joints. Int J Plast 2022;155:103308.
[33] Long X, Hu B, Feng YH, Chang C, Li MY. Correlation of microstructure and constitutive behaviour of sintered silver particles via nanoindentation. Int J Mech Sci 2019;161:105020.
[34] Long X, Jia QP, Shen ZY, Liu M, Guan C. Strain rate shift for constitutive behaviour of sintered silver nanoparticles under nanoindentation. Mech Mater 2021;158.
[35] Long X, Jia QP, Li Z, Wen SX. Reverse analysis of constitutive properties of sintered silver particles from nanoindentations. Int J Solids Struct 2020;191:351–62.
[36] Long X, Shen ZY, Jia QP, Li J, Dong RP, Su YT, et al. Determine the unique constitutive properties of elastoplastic materials from their plastic zone evolution under nanoindentation. Mech Mater 2022;175:104485.
[37] Zhao S, Dai YW, Qin F, Li YN, An T, Gong YP. Effect of surface finish metallization layer on shearing fracture toughness of sintered silver bonded joints. Engng Fract Mech 2022;264:108355.

[38] Lee B-S, Yoon J-W. Die-attach for power devices using the Ag sintering process: interfacial microstructure and mechanical strength. Metals Mater Int 2017;23(5): 958–63.

[39] Kim D, Lee S, Chen CT, Lee S-J, Nagao S, Suganuma K. Fracture mechanism of microporous Ag-sintered joint in a GaN power device with Ti/Ag and Ni/Ti/Ag metallization layer at different thermo-mechanical stresses. J Mater Sci 2021;56(16):9852–70.

[40] Huang Z, Kumar P, Dutta I, Pang J, Sidhu R, Renavikar M, et al. Fracture of Sn-Ag-Cu solder joints on Cu substrates: I. effects of loading and processing conditions. J Electron Mater 2012;41(2):375–89.

[41] Chen CT, Nagao S, Suganuma K, Jiu JT, Sugahara T, Zhang H, et al. Macroscale and microscale fracture toughness of microporous sintered Ag for applications in power electronic devices. Acta Mater 2017;129:41–51.

[42] Kim M-S, Nishikawa H. Effects of bonding temperature on microstructure, fracture behavior and joint strength of Ag nanoporous bonding for high temperature die attach. Mater Sci Eng: A 2015;645:264–72.

[43] Zhu J.Q, Su Y.T, Chen C.T, SIOW K.S, Tang R.T, Long X. Porosity effect on fracture behavior of sintered silver nanoparticles by phase-field modeling. in 2021 IEEE 23rd Electronics Packaging Technology Conference (EPTC). 2021. IEEE.

[44] Su YT, Fu GC, Liu CQ, Zhang K, Zhao LG, Liu CY, et al. Thermo-elasto-plastic phase-field modelling of mechanical behaviours of sintered nano-silver with randomly distributed micro-pores. Computer Methods in Appl Mechan Eng 2021;378:113729.

[45] Su YT, Fu GC, Liu CQ, Liu CY, Long X. Fatigue crack evolution and effect analysis of Ag sintering die-attachment in SiC power devices under power cycling based on phase-field simulation. Microelectron Reliab 2021;126:114244.

[46] Roters F, Eisenlohr P, Hantcherli L, Tjahjanto DD, Bieler TR, Raabe D. Overview of constitutive laws, kinematics, homogenization and multiscale methods in crystal plasticity finite-element modeling: theory, experiments, applications. Acta Mater 2010;58(4):1152–211.

[47] Huang Y, A user-material subroutine incroporating single crystal plasticity in the ABAQUS finite element program. 1991: Harvard Univ. Cambridge, UK.

[48] Asaro R.J, Needleman A, *Overview no. 42 texture development and strain hardening in rate dependent polycrystals.* Acta metallurgica, 1985. **33**(6): p. 923-953.

[49] Hutchinson J.W, *Bounds and self-consistent estimates for creep of polycrystalline materials.* Proceedings of the Royal Society of London. A. Mathematical Physical Sciences, 1976. **348**(1652): p. 101-127.

[50] Canadinc D, Sehitoglu H, Maier H, Chumlyakov Y. Strain hardening behavior of aluminum alloyed Hadfield steel single crystals. Acta Mater 2005;53(6): 1831–42.

[51] Asaro RJ. Micromechanics of crystals and polycrystals. Adv Appl Mech 1983;23:1–115.

[52] Nygårds M, Gudmundson P. Three-dimensional periodic Voronoi grain models and micromechanical FE-simulations of a two-phase steel. Comput Mater Sci 2002;24(4):513–9.

[53] Benedetti I, Aliabadi MH. A three-dimensional grain boundary formulation for microstructural modeling of polycrystalline materials. Comput Mater Sci 2013; 67:249–60.

[54] Aurenhammer FJ. Voronoi diagrams—a survey of a fundamental geometric data structure. ACM Comput Surv 1991;23(3):345–405.

[55] Qian C, Gu T, Wang P, Cai W, Fan XJ, Zhang GQ, et al. Tensile characterization and constitutive modeling of sintered nano-silver particles over a range of strain rates and temperatures. Microelectron Reliab 2022;132:114536.

[56] Zhang L, Zhao LG, Jiang R, Bullough C. Crystal plasticity finite-element modelling of cyclic deformation and crack initiation in a nickel-based single-crystal superalloy under low-cycle fatigue. Fatigue Fracture of Eng Mater Struct 2020;43(8):1769–83.

[57] Zhang K-S, Shi Y-K, Ju JW. Grain-level statistical plasticity analysis on strain cycle fatigue of a FCC metal. Mech Mater 2013;64:76–90.

[58] Qiu ZJ, Zhao WJ, Cao MK, Wang YQ, Lam JW, Zhang Z, et al. Dynamic visualization of stress/strain distribution and fatigue crack propagation by an organic mechanoresponsive AIE luminogen. Adv Mater 2018;30(44):1803924.

[59] Lin B, Zhao LG, Tong J. A crystal plasticity study of cyclic constitutive behaviour, crack-tip deformation and crack-growth path for a polycrystalline nickel-based superalloy. Engng Fract Mech 2011;78(10):2174–92.

[60] Benedetti I, Gulizzi V. A grain-scale model for high-cycle fatigue degradation in polycrystalline materials. Int J Fatigue 2018;116:90–105.

[61] Li Z, Yang F. Grain rotations during uniaxial deformation of gradient nano-grained metals using crystal plasticity finite element simulations. Extreme Mech Lett 2017;16:41–8.